Crack onset and propagation stability from a circular hole under biaxial loading

Crack onset and propagation stability from a circular hole under biaxial loading

A. Sapora [a]*, P. Cornetti[a]

[a] *Department of Structural, Geotechnical and Building Engineering, Politecnico di Torino, Corso Duca degli Abruzzi 24, 10129, Torino, Italy*

* Corresponding Author: alberto.sapora@polito.it

Abstract

The brittle crack initiation from a circular hole in an infinite slab subjected to remote biaxial loading is investigated by means of **the coupled Finite Fracture Mechanics criterion, focussing on the behaviour of the average energy release rate. The work then analyzes the stability/instability of crack growth**, following the terminology put forward by [Weißgraeber, P., Hell, S., Becker, W. (2016), Engineering Fracture Mechanics, 168, 93–104]. Depending on the loading biaxiality and on the ratio between the crack advance and the hole radius, the crack propagation could reveal to be either unstable (positive geometries), or stable (negative geometries). Furthermore, it is shown that stable paths could follow unstable paths and vice-versa, leading to locally positive/globally negative **or locally negative/globally positive configurations**, which are discussed in detail case by case.

Keywords: Circular hole, biaxial loading, crack onset, energy release rate, Finite Fracture Mechanics, instability.

1. Introduction

Linear Elastic Fracture Mechanics (LEFM) classifies structural configurations into two main categories, e.g. (Bazant and Planas 1998): positive and negative geometries, respectively. According to the former ones, the strain energy release rate (ERR) associated to an infinitesimal crack growth is a monotonically increasing function, and this leads to an unstable crack growth. In the latter case, the ERR shows a monotonically decreasing behaviour, giving rise to a stable crack propagation. As a consequence, the load associated to the subsequent nucleation step increases.

Regarding the brittle crack onset, whereas LEFM was found to provide good results for structures containing sufficiently large cracks, when dealing with notched structures the approach presents several drawbacks and the related predictions are unreliable (Taylor et al. 2005, Taylor 2007). This is one of the reasons according to which Finite Fracture Mechanics (FFM) was introduced (Leguillon

2002, **Taylor et al. 2005**, **Cornetti et al. 2006**, Carpinteri et al. 2008). The basic assumption of FFM is that the fracture propagates by a finite crack extension, whose value is one of the output of two coupled conditions: an energetic requirement, involving the average ERR, and a stress constraint, involving the average stress field in front of the notch tip. The FFM crack advance is not a material function (as it happens for common criteria based on a critical distance (Taylor 2007)), but a structural parameter, thus depending on the geometry under investigation. Once the crack is nucleated, the crack propagation is governed by **LEFM, which can be considered the limit case of FFM as the crack extension becomes infinitesimal.**

Weißgraeber et al. (2016) **have recently discussed on the stability/instability of crack growth after the FFM crack onset**, distinguishing between negative geometries, globally negative/locally positive geometries, and globally positive/locally negative geometries. By the way, three different structural configurations were analyzed, one for each of the above behaviours: a point loaded centre crack, a point loaded open-hole, and an adhesively bonded single lap joint.

In the present study a similar analysis will be carried out through FFM (Carpinteri et al. 2008), but based on a single geometry: a circular hole in an infinite plate under remote biaxial loading (Fig. 1). Indeed, the loading parameter λ recovers a crucial role in determining the condition for the crack initiation at the hole edge and the stability of the crack **propagation**, covering all the possible situations in a synthetic but exhaustive way.

1. Circular hole in an infinite slab

Let us consider a circular hole of radius *R* in an infinite slab subjected to remote biaxial loading as depicted in Fig. 1. The stress intensity factor (SIF) function related to a crack of length *a* stemming from the hole can be approximated according to the following expression (Tada et al. 2000)

$$K_I(\tilde{a}) = \sigma\sqrt{\pi R\tilde{a}}\,F(s) \tag{1}$$

where $\tilde{a} = a/R$ is the dimensionless crack length and $s = \tilde{a}/(\tilde{a}+1)$.

The shape function *F* related to a symmetric crack propagation (Fig. 1), preferred for this geometry to the asymmetric one (Sapora et al. in 2018), can be expressed as:

$$F(s) = (1-\lambda)F_0(s) + \lambda F_1(s) \tag{2}$$

where

$$F_0(s) = 0.5\,(3-s)\,[1+1.243(1-s)^3] \tag{3a}$$

$$F_1(s) = 1 + (1-s)\,[0.5 + 0.743(1-s)^2] \tag{3b}$$

The accuracy of Eqs. (2-3) was estimated to be better than 1% by Tada et al. (2000).

1.1 Finite Fracture Mechanics

The coupled criterion of FFM (Cornetti et al. 2006; Carpinteri et al. 2008) is based on the simultaneous fulfilment of two requirements. The **first** is the energy balance: the average ERR must be greater than the fracture energy. By means of Irwin's relationship, this condition can be expressed in terms of the SIF (1) and the fracture toughness K_{Ic} as

$$\bar{K}(\tilde{\Delta}) = \sqrt{\frac{1}{\tilde{\Delta}}\int_0^{\tilde{\Delta}} K_I^2(\tilde{a})\,d\tilde{a}} \geq K_{Ic} \tag{4}$$

$\tilde{\Delta} = \Delta / R$ being the dimensionless crack advance.

The **second** is a stress requirement, according to which the average circumferential stress in front of the hole edge must be greater than the tensile strength σ_u:

$$\bar{\sigma}(\tilde{\Delta}) = \frac{1}{\tilde{\Delta}}\int_1^{1+\tilde{\Delta}} \sigma_y(\tilde{x})\,d\tilde{x} \geq \sigma_u \tag{5}$$

where $\tilde{x} = x / R$. For what concerns the geometry under investigation (Fig. 1), the stress field according to Kirsch (1898) writes:

$$\sigma_y(\tilde{x}) = \frac{\sigma}{2}\left[2 + \frac{(1+\lambda)}{\tilde{x}^2} + 3\frac{(1-\lambda)}{\tilde{x}^4}\right] \tag{6}$$

leading to the following stress concentration factor:

$$\frac{\sigma_y^{\max}(\tilde{x}=1)}{\sigma} = 3 - \lambda \tag{7}$$

The analysis will be restricted to the case λ < 1, so that the highest tensile stress is always attained at the interception of the hole edge with the *x*-axis, which defines the point of crack onset. Correspondingly, the stress field $\sigma_y(\tilde{x})$ (Eq. (6), and thus the function $\bar{\sigma}(\tilde{\Delta})$ expressed by Eq. (5)) is a monotonically decreasing function. On the contrary, the loading conditions affect significantly the behaviour of the SIF $K_I(\tilde{a})$ (Eq. (1)) and thus of the average function $\bar{K}(\tilde{\Delta})$ (Eq. (4)).

2 Crack onset and stability discussion

Once the crack onset is predicted by FFM, LEFM can be reasonably supposed to govern the subsequent crack growth. The condition for stability upon crack propagation is thus based on the sign of the derivative dK_I / da: if $dK_I / da > 0$ the crack growth is unstable, whereas if $dK_I / da < 0$ it reveals to be stable. The particular case $dK_I / da = 0$ has to be treated separately, and the related classification depends on the sign of the higher order derivatives. By referring to Fig. 1, three different situations will be investigated in the following corresponding to uniaxial tension, uniaxial compression, and biaxial loading, respectively.

2.1 Uniaxial tension

In case of uniaxial tension (λ=0), the SIF $K_I(\tilde{a})$ (Eq. (1)) is a monotonically increasing function (and so $\bar{K}(\tilde{\Delta})$, (Eq. (4))), leading to a positive geometry. At incipient failure ($\sigma = \sigma_f$), the FFM criterion thus reverts to a system of two equations in two unknowns: the critical crack advance $\tilde{\Delta}_c = \Delta_c / R$ and the failure stress $\tilde{\sigma}_f = \sigma_f / \sigma_u$. In formulae:

$$\begin{cases} \bar{\sigma}(\tilde{\Delta}_c) = \dfrac{1}{\tilde{\Delta}_c} \displaystyle\int_1^{1+\tilde{\Delta}_c} \sigma_y(\tilde{x}) d\tilde{x} = \sigma_u \\ \bar{K}(\tilde{\Delta}_c) = \sqrt{\dfrac{1}{\tilde{\Delta}_c} \displaystyle\int_0^{\tilde{\Delta}_c} K_I^2(\tilde{a}) d\tilde{a}} = K_{Ic} \end{cases} \tag{8}$$

The subsequent crack propagation is always unstable ($dK_I / d\tilde{a} > 0$), and thus the crack initiation coincides with the collapse of the structure. This case (i.e., positive geometries) will not be analyzed further here, since it corresponds to common configurations where the FFM criterion has been already applied successfully. **By introducing the well-known Irwin's length $l_{ch} = \left(K_{Ic} / \sigma_u\right)^2$, the comparison between the FFM failure stress and the experimental data obtained by carrying out *ad-hoc* tensile tests on PMMA and GPPS samples (Sapora et al. 2018) is shown in Fig. 2**. For other recent studies on circular holes see, for instance, (Camanho et al. 2012, Furtado et al. 2017, Rosendahl et al. 2017).

2.2 Uniaxial compression

The case of uniaxial compression can be treated by exploiting the principle of effect superposition, i.e. by setting λ=−1 and subtracting to this geometry that corresponding to λ=0 (Fig. 1). This leads to the following shape function *F* (Eq. (2)):

$$F(s) = F_0(s) - F_1(s) \tag{9}$$

and the following stress field along the *x* axis **(Eq. (6))**:

$$\sigma_y(\tilde{x}) = \frac{\sigma}{2}\left[-\frac{1}{\tilde{x}^2} + \frac{3}{\tilde{x}^4}\right] \tag{10}$$

The function $\bar{K}(\tilde{\Delta})$ (Eq. (4)) is plotted in Fig. 3, revealing a maximum for $\tilde{\Delta} = \tilde{\Delta}^* \simeq 0.31$. Denoting the generic solution of system (8) by $\tilde{\Delta}_s$ without loss of generality, two situations can thus occur:

1) $\tilde{\Delta}_s < \tilde{\Delta}^*$: in such a case $\tilde{\Delta}_c = \tilde{\Delta}_s$. The FFM criterion (4,5) is actually expressed by system (8). **The generated crack is unstable (**$dK_I / da > 0$**,** Fig. 3**), but** after some extensions the propagation will turn to be stable as described in point 2.
2) $\tilde{\Delta}_s \geq \tilde{\Delta}^*$: in such a case $\tilde{\Delta}_c = \tilde{\Delta}^*$. No cracks with length $\tilde{\Delta}_c > \tilde{\Delta}^*$ can develop, since they would correspond to a higher crack onset load with respect to that occurring for $\tilde{\Delta}_c = \tilde{\Delta}^*$. The FFM criterion is thus expressed by imposing $\tilde{\Delta}_c = \tilde{\Delta}^*$ in the energy requirement (4), and letting increase the failure stress in order to achieve $\bar{K} = K_{Ic}$ (Mantič 2009, Weißgraeber et al. 2016):

$$\bar{K}(\tilde{\Delta}^*) = \sqrt{\frac{1}{\tilde{\Delta}^*}\int_0^{\tilde{\Delta}^*} K_I^2(\tilde{a})\,d\tilde{a}} = K_{Ic} \tag{11}$$

In this case, the stress requirement (5) is trivially (over) fulfilled. Of course, **after the (finite) crack onset, the (infinitesimal) crack growth reveals to be stable (**$K_I(\tilde{a})$ **being monotonically decreasing, Fig. 3) and described by LEFM.**

The behavior described above was referred to as locally positive/globally negative by Weißgraeber et al. (2016). **A similar situation can be found in debonding onset problems in spherical-particle-reinforced composites subjected to uniaxial remote tension (Garcia et al. 2015).**

FFM predictions are plotted in Figure 4. Both the nucleation stress $\hat{\sigma}_f = \sigma_f / \sigma_u$ and the crack advance $\hat{\Delta}_c = \Delta_c / l_{ch}$ present a dimensionless hole radius $\hat{R}^* = R^* / l_{ch} \simeq 1.44$ (corresponding to $\tilde{\Delta}^* \simeq 0.31$) **above which (**$\tilde{\Delta}_c = \tilde{\Delta}_s < \tilde{\Delta}^*$**) the solution is obtained by the coupled system (8). Below**

$\hat{R}^*$ **(**$\tilde{\Delta}_s \geq \tilde{\Delta}^*$) the FFM criterion reverts to the energy condition (11). **Consequently, the failure load is proportional to** $1/\sqrt{\hat{R}^*}$**,** and $\hat{\Delta}_c = \Delta_c / l_{ch}$ is a linear function of $\hat{R}^*$ **as can be easily detected from Eq. (1). This a typical behaviour when solely the energy condition governs the crack nucleation, as firstly observed by Mantič (2009): according to his terminology, the quantity** $1/\sqrt{\hat{R}^*}$ **was referred to as brittleness number**. The deviation from predictions described by the coupled system in this range (dash-dotted line in Fig. 4) is significant, although the propagation is stable. Finally, note that for sufficiently high $\hat{R}^*$ the solution is stress governed ($\hat{\sigma}_f \to 1$), being the stress field constant and equal to σ , and the energy balance only provides the crack advance, $\hat{\Delta}_c \to 2/\left(\pi 1.12^2\right) \simeq 0.507$ (Carpinteri et al. 2008).

The comparison between FFM predictions on the nucleation stress and experimental data on Tyndall Stone and Vanscoy Potash obtained by Carter et al. (1992) is reported in Fig. 5, by implementing the material properties presented in Leguillon et al. (2007). Similar plots were obtained also by Leguillon et al. (2007) and Lecampion (2012), although through different approaches from the present FFM one.

2.3 Biaxial loading

As concerns the case of biaxial loading with λ <1, we could further distinguish between two situations according to the values of λ: the range $-2.6 \leq \lambda < 1$ leads to positive geometries, and the situation is thus similar to that described in Section 2.1 in case of tensile loading ($\lambda = 0$).

In order to investigate the range $\lambda < -2.6$ (**which leads to biaxial tension-compression, Fig. 1**), the diagram of $\bar{K}$ as function of $\tilde{\Delta}$ is plotted in Fig. 6 by assuming, e.g., $\lambda = -6$. The $\bar{K}(\tilde{\Delta})$ function is firstly increasing from 0 to $\tilde{\Delta}^*$, then decreasing up to a local minimum, and finally increasing indefinitely. Two significant crack advances are present: $\tilde{\Delta}^*$ (corresponding to the relative maximum of $\bar{K}$) and $\tilde{\Delta}^{**}$ (according to which $\bar{K}(\tilde{\Delta}^*) = \bar{K}(\tilde{\Delta}^{**})$). The situation can be described as follows:

1) $\tilde{\Delta}_s < \tilde{\Delta}^*$: in such a case $\tilde{\Delta}_c = \tilde{\Delta}_s$. According to FFM there exists a dimensionless radius $\hat{R}^*$ corresponding to $\tilde{\Delta}^*$ above which ($\hat{R} > \hat{R}^*$, Fig. 7) the criterion is described by the coupled equations (8)**. The subsequent infinitesimal crack growth reveals to be unstable, up to a possible stable phase as described in point 2.**

2) $\tilde{\Delta}^* \le \tilde{\Delta}_s < \tilde{\Delta}^{**}$: in such a case $\tilde{\Delta}_c = \tilde{\Delta}^*$. The FFM criterion is expressed by means of Eq. (11) ($\hat{R}^{**} \le \hat{R} < \hat{R}^*$, Fig. 7), thus imposing $\tilde{\Delta}_c = \tilde{\Delta}^*$ in the energy condition (4), being the stress condition (5) overfulfilled. This case is reported in Fig. 8a for $\hat{R} = 0.5$: the minimum failure load which satisfies both the stress and the energy conditions (Eqs. (4) and (5), respectively) coincides with the minimum of the energy curve. Indeed, the deviation from predictions by Eq. (8) is not so significant in this range, at least if referred to the critical stress $\tilde{\sigma}_f$. A stronger variation is observed for the crack advancement, $\hat{\Delta}_c$ being a linear function of $\hat{R}$. On the other hand, after a stable crack growth governed by LEFM (see the diagram of $K_I(\tilde{a})$ in Fig. 6), an unstable propagation is expected. **When passing from the stable branch to the unstable one, the situation is similar to that of the initial crack onset, and the transition could be ruled by FFM once more. Further studies are in progress.**

3) $\tilde{\Delta}_s \ge \tilde{\Delta}^{**}$: in such a case $\tilde{\Delta}_c = \tilde{\Delta}_s$. In this range (corresponding to $\hat{R} \le \hat{R}^{**}$ in Fig. 7) it is legitimate to apply the FFM system (8): the minimum failure load coincides with the intersection point of the stress and energy curves (Fig. 8b for $\hat{R} = 0.05$). **After nucleation, the crack results to be definitely unstable (** $dK_I / da > 0$ **).**

This kind of behaviour was referred to as locally negative/globally postive by Weißgraeber et al. (2016). Indeed, this structural configuration is often met in practical cases such as a crack approaching the interfaces of two materials (Leguillon and Martin 2013a,b), or crack initiation in adhesive joints (Hell et al. 2014).

It is also interesting to point out that, in case of biaxial loading, the extreme cases are dominated by the stress condition (5), whereas the energy balance (4) provides merely the crack advance. Indeed, the stress field is constant and equal to σ for $\hat{R} = 0$, yielding $\tilde{\sigma}_f = 1$, and $\tilde{\Delta}_c = 2/\pi \simeq 0.637$. Furthermore, as $\hat{R} \to \infty$, the asymptotic stress field tends to the constant value $(3–\lambda)\sigma$: thus $\tilde{\sigma}_f \to 1/(3-\lambda)$, and $\tilde{\Delta}_c \to 2/\left(\pi 1.12^2\right) \simeq 0.507$.

Of course the values of $\tilde{\Delta}^*, \hat{R}^*$ and $\tilde{\Delta}^{**}, \hat{R}^{**}$ depend on the parameter λ: as it decreases, $\tilde{\Delta}^*$ tend to 0.31 and $\hat{R}^*$ to 1.44, whereas $\tilde{\Delta}^{**}$ diverges and $\hat{R}^{**}$ tends to zero. In other words, as $\lambda \to -\infty$ the distance between $\hat{R}^{**}$ and $\hat{R}^*$ increases (Fig. 9), and the limits for the case of compressive loading (Section 2.2) are qualitatively recovered.

Finally, it is interesting to outline an interesting implication of the present results. As long as the ratio between the hole and the specimen diameters keeps low (thus recovering the case of an infinite geometry), the structural configuration of Brazilian disk (BD) samples containing a circular notch is similar to that investigated (Fig. 1) by setting λ=–3 (Torabi et al. 2017): the stress field and the SIF functions in the neighbourhood of the hole edge can be thus expressed by means of Eqs. (1) and (6), without loss of accuracy.

Indeed, BD tests on circularly notched samples were carried out by Torabi et al (2017). Two different materials (PMMA and GPPS, respectively, both corresponding to $l_{ch} \simeq 0.5\,\text{mm}$) and five hole radii, namely *R*= 4, 2, 1, 0.5, 0.25 mm, were involved in the experimental campaign. Note that the smallest hole corresponds to $\hat{R} \simeq 0.5$, which is comprised between $\hat{R}^{**} \simeq 0.24$ and $\hat{R}^{*} \simeq 0.68$ for λ=–3 (Fig. 9). From a rigorous point of view, FFM predictions should have been obtained by means of Eq. (11). On the other hand, this aspect was disregarded in the theoretical analysis and Eq. (8) was implemented instead (Torabi et al. 2017). The committed error is not so significant in terms of failure stress (see the true FFM curve in Fig. 10, indeed the geometrical correction factor implemented by Torabi et al. 2017) has not been taken into account), but a relevant deviation could have been detected in terms of the critical crack advance, which unfortunately was not measured experimentally.

In order to stress this behaviour, it would be interesting to carry out similar tests by reducing $\hat{R}$: since machining smaller hole diameters could result in a difficult task, this means considering a material less brittle (increasing thus l_{ch}) than GPPS or PMMA .

3. Conclusions

The loading parameter λ<1 and the dimensionless hole radius $\hat{R} = R / l_{ch}$ govern both the FFM crack onset from a circular hole subjected to biaxial loading, and the subsequent LEFM propagation stability. More specifically:

- for λ > –2.6, $\bar{K}_I(\tilde{\Delta})$ is a monotonically increasing function: this is the configuration of positive geometries, **and the nucleated crack is always unstable**
- for λ < –2.6, **there exist two dimensionless radii $\hat{R}^{**}$ and $\hat{R}^{*}$, with $\hat{R}^{**} < \hat{R}^{*}$, below and above which the crack growth is (locally) unstable; in between it is stable.** The distance between the two values of $\hat{R}^{**}$ and $\hat{R}^{*}$ decreases with λ. This is the case of locally negative/globally positive geometries: after some possible stable crack extensions, an unstable propagation will definitely take place;

- as $\lambda \to -\infty$ it follows that $\hat{R}^{**} \to 0, \hat{R}^{*} \to 1.44,$ and the case of uniaxial compressive loading is recovered: the crack propagation after onset is (locally) unstable for $\hat{R}$ >1.44, stable otherwise.

For each of the above cases, the FFM predictions were compared successfully with the experimental data available in the Literature (Carter et al. 1992, Torabi et al. 2017, Sapora et al. 2018**), restricting the analysis to the nucleation/failure stress, since the initiation crack length was not measured during tests. As concerns the stable/unstable behaviour related to the subsequent crack growth, a more accurate study could be performed by means of a finite element simulation, which would allow the exact evaluation of the stress field to be implemented.**

References

Bažant, Z.P., Planas, J. (1998). Fracture and Size Effect in Concrete and Other Quasibrittle Materials. CRC press, London.

Camanho, P.P., Erçin, G., Catalanotti, G., Mahdi, D., Linde, P. (2012). A finite fracture mechanics model for the prediction of the open-hole strength of composite laminates, *Composites Part A: Applied Science and Manufacturin*g **43**, 1219–1225.

Carpinteri, A., Cornetti, P., Pugno, N., Sapora, A., Taylor, D. (2008). A finite fracture mechanics approach to structures with sharp V-notches, *Eng Fract Mech* **75**, 1736–1752.

Cornetti, P., Pugno, N., Carpinteri, A., Taylor, D. (2006). Finite fracture mechanics: a coupled stress and energy failure criterion. *Eng Fract Mech* **73**, 2021–33.

Carter B.J., Lajtai, E.Z., Yuan, Y. (1992). Tensile fracture from circular cavities loaded in compression. *Int J Fract*, **57**, 221–236.

Furtado, C., Arteiro, A., Bessa, M.A., Wardle, B.L., Camanho, P.P. (2017). Prediction of size effects in open-hole laminates using only the Young's modulus, the strength, and the R-curve of the 0° ply, *Composites Part A: Applied Science and Manufacturing*, **101**, 306-317.

García, I., Mantic, V., Graciani, E. (2015). A model for the prediction of debond onset in spherical-particle-reinforced composites under tension. Application of a coupled stress and energy criterion. *Compos Sci Technol* **106**, 60–7.

Hell S, Weißgraeber P, Felger J, Becker W. (2014). A coupled stress and energy criterion for the assessment of crack initiation in single lap joints: a numerical approach. *Eng Fract Mech* **117**:112–26.

Kirsch, E.G. (1898). Die Theorie der Elastizität und die Bedürfnisse der Festigkeitslehre, *Zeitschrift des Vereines deutscher Ingenieure*, **42**, 797-807.

Lecampion, B. (2012). Modeling size effects associated with tensile fracture initiation from a wellbore. *International Journal of Rock Mechanics & Mining Sciences*, **56**, 67–76.

Leguillon, D. (2002). Strength or toughness? A criterion for crack onset at a notch. *Eur J Mech A/Solids*, **21**, 61‑72.

Leguillon, D., Martin, E. (2013a). The strengthening effect caused by an elastic contrast—Part I: the bimaterial case. *Int J Fract*, **179**, 157–67.

Leguillon, D., Martin, E. (2013b). The strengthening effect caused by an elastic contrast—Part II: stratification by a thin stiff layer. *Int J Fract*, **179**, 169-178.

Leguillon, D., Quesada, D., Putot, C., Martin, E. (2007). Prediction of crack initiation at blunt notches and cavities: size effects. *Eng Fract Mech*, **74**, 2420–36.

Mantič, V. (2009). Interface crack onset at a circular cylindrical inclusion under a remote transverse tension. Application of a coupled stress and energy criterion. *International Journal of Solids and Structures* 46, 287-1304.

Rosendahl, P.L., Weißgraeber, P., Stein, N., Becker, W. (2017). Asymmetric crack onset at open-holes under tensile and in-plane bending loading. *Int J Solids Struct*, **113–114**, 10-23.

Sapora, A., Torabi, A.R., Etesam, S., Cornetti, P. (2018). Finite Fracture Mechanics crack initiation from a circular hole, *Fatigue Fract Eng Mater Struct*, **41**, 1627–1636.

Tada, H., Paris, P., Irwin, G. (2000). The Stress Analysis of Cracks Handbook. Third Edition, Paris Productions Incorporated, St Louis, MO, USA.

Taylor, D. (2007). The Theory of Critical Distances: a New Perspective in Fracture Mechanics, Elsevier: Oxford, UK.

Taylor, D., Cornetti, P., Pugno, N. (2005). The fracture mechanics of finite crack extension, *Eng Fract Mech* **72**,1021–1038.

Torabi, A.R., Etesam, S., Sapora, A., Cornetti, P. (2017). Size effects on brittle fracture of Brazilian disk samples containing a circular hole, *Eng Fract Mech* **186**, 496‑503.

Weißgraeber, P., Hell, S., Becker, W. (2016). Crack nucleation in negative geometries, *Eng Fract Mech* **168**, 93–104.

Figure Caption

Fig. 1. Circular hole in an infinite slab subjected to remote biaxial loading.

Fig. 2. **Uniaxial tension**: FFM failure stress and experimental data obtained by Sapora et al. (2018).

Fig. 3. **Uniaxial compression**: $K_I(\tilde{a})$ and $\bar{K}(\tilde{\Delta})$ functions.

Fig. 4. **Uniaxial compression**: FFM nucleation stress (and crack advance in the upper-right corner) vs. hole radius. For $\hat{R} < \hat{R}^*$ the FFM solution is provided by Eq. (11) (continuous thick line; the dash-dot line refers to predictions by Eq. (8) in this range). For $\hat{R} \geq \hat{R}^*$ the FFM solution is provided by Eq. (8) (continuous line).

Fig. 5. Uniaxial compression: FFM nucleation stress and experimental data obtained by Carter et al. (1992).

Fig. 6. Biaxial loading ($\lambda = -6$): $K_I(\tilde{a})$ and $\bar{K}(\tilde{\Delta})$ functions.

Fig. 7. Biaxial loading ($\lambda = -6$): FFM nucleation/failure stress (and crack advance in the upper-right corner) vs. hole radius. If $\hat{R} < \hat{R}^*$ or $\hat{R} \geq \hat{R}^*$ the FFM solution is provided by system (8) (continuous line). If $\hat{R}^* \leq \hat{R} < \hat{R}^{**}$ the FFM criterion is governed by the energy condition alone (11) (continuous thick line; the dash-dotted line refers to predictions by Eq. (8) in this range).

Fig. 8. Biaxial loading ($\lambda = -6$): FFM nucleation/failure stress (circle) for $\hat{R} = 0.5$ (a) and $\hat{R} = 0.05$ (b). In both figures, the FFM prediction is the minimum value satisfying both the stress requirement (5) (area above the continuous thick line) and the energy requirement (4) (area above the continuous line).

Fig. 9. $\hat{R}^*$ and $\hat{R}^{**}$ values vs. loading parameter λ.

Fig. 10. Biaxial loading ($\lambda = -3$): FFM nucleation/failure stress and experimental data obtained by Torabi et al. (2017).

Fig. 1

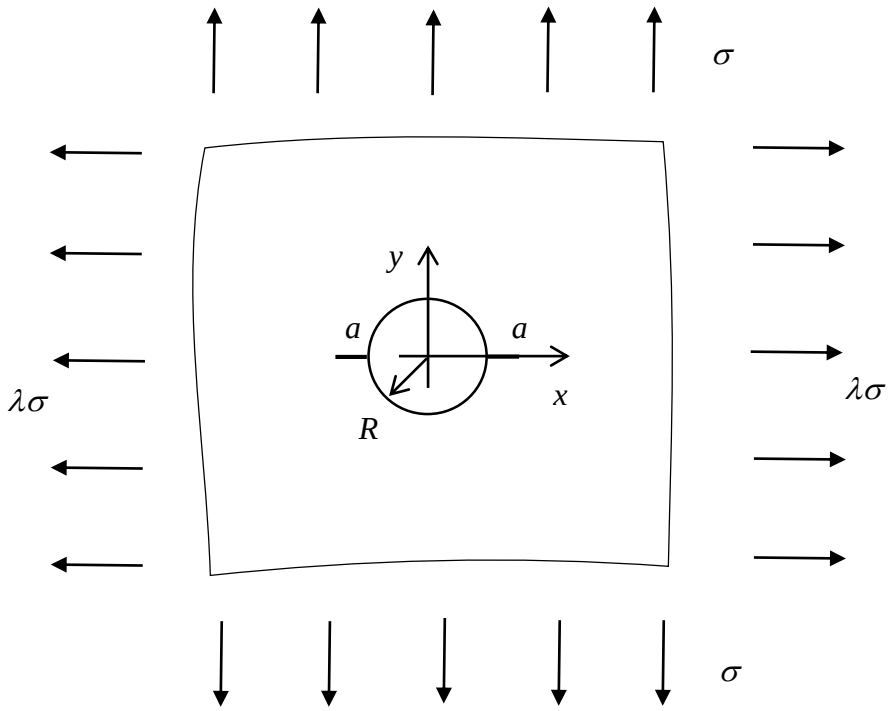

Fig. 3

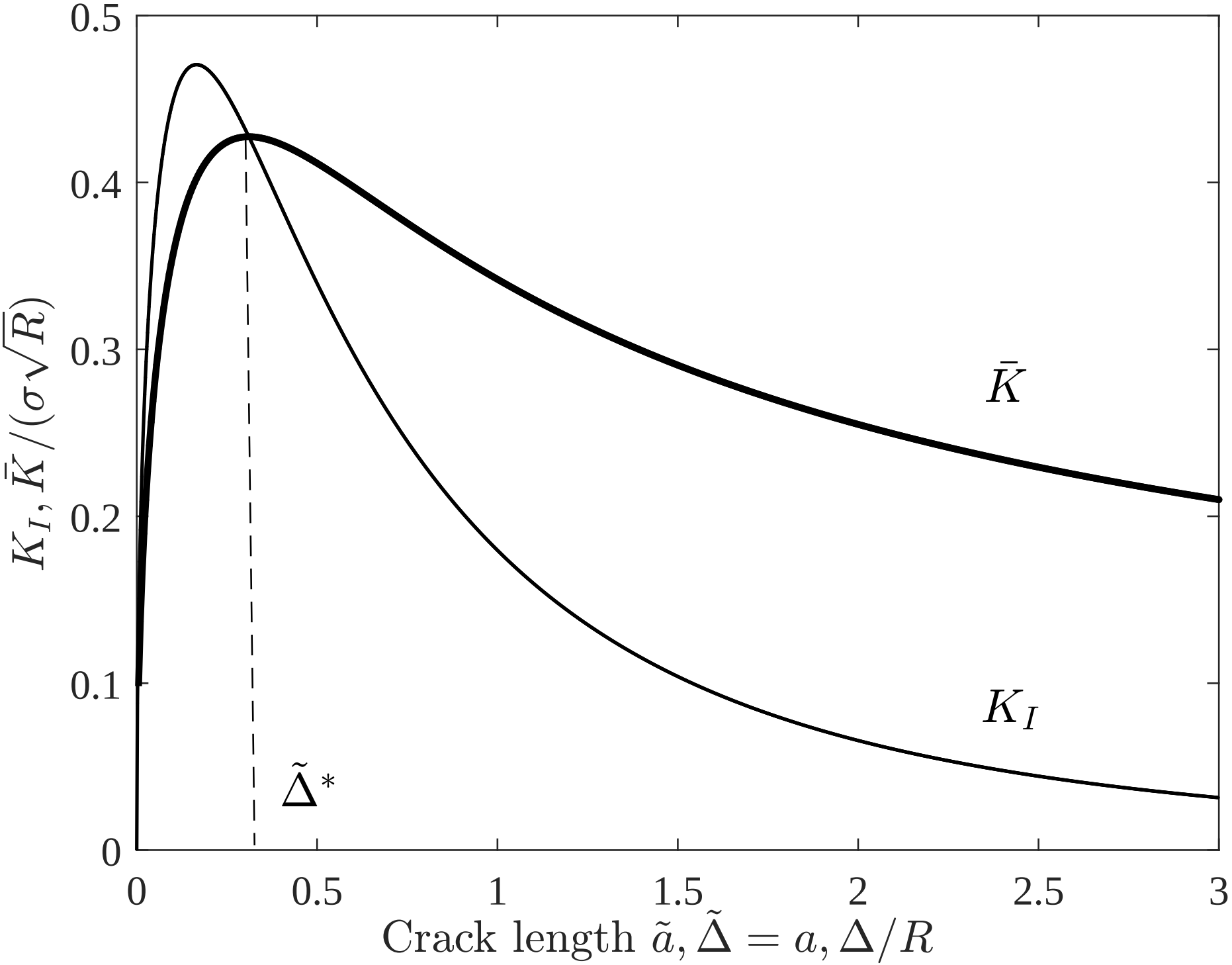
0.5
0.4
0.3
0.2
0.1
0
$K_I, \bar{K}/(\sigma\sqrt{R})$
$\bar{K}$
K_I
$\tilde{\Delta}^*$
0
0.5
1
1.5
2
2.5
3
Crack length $\tilde{a}, \tilde{\Delta} = a, \Delta/R$

Fig. 2

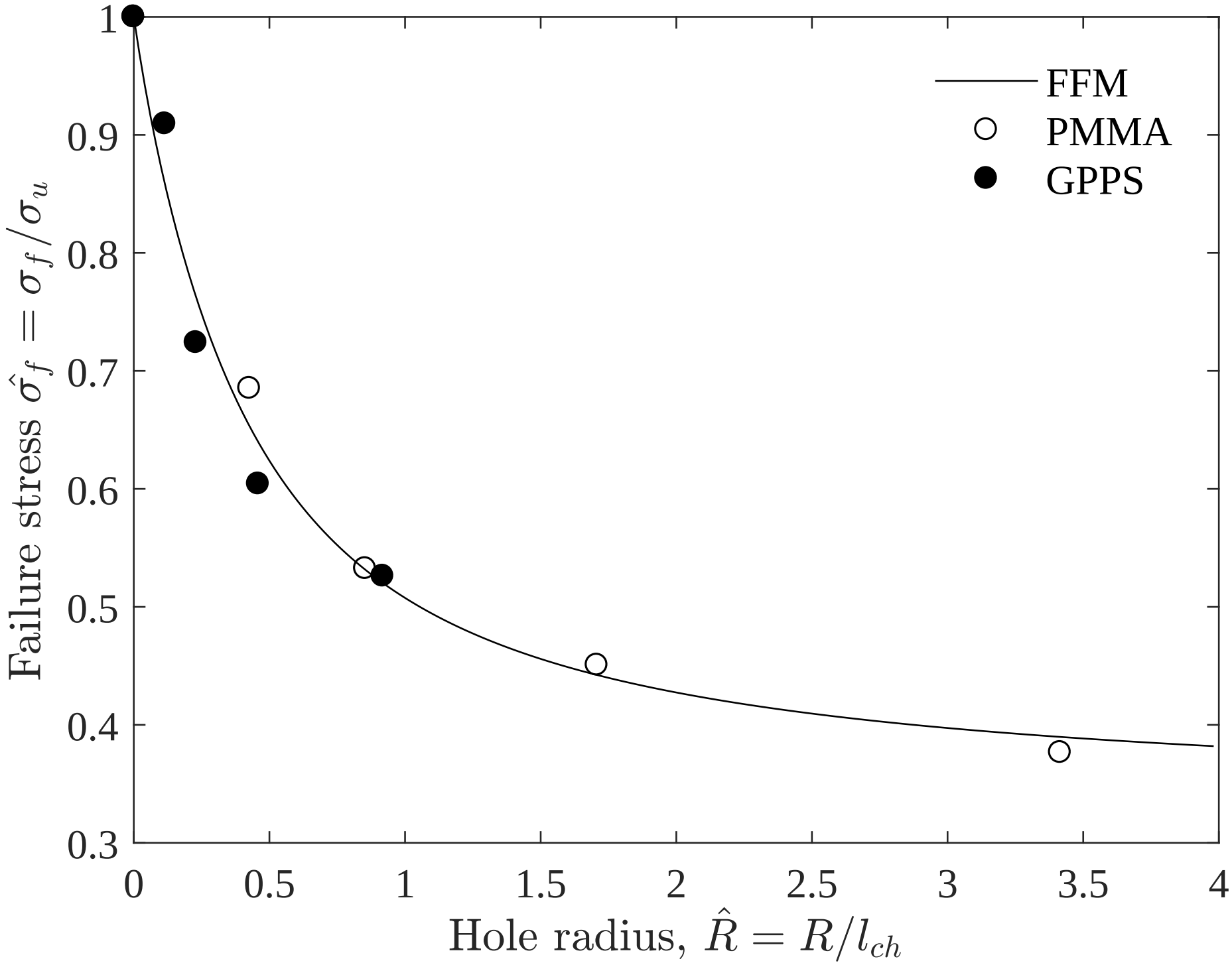
FFM
PMMA
GPPS
Failure stress $\hat{\sigma}_f = \sigma_f/\sigma_u$
Hole radius, $\hat{R} = R/l_{ch}$
1
0.9
0.8
0.7
0.6
0.5
0.4
0.3
0
0.5
1
1.5
2
2.5
3
3.5
4

Fig. 4

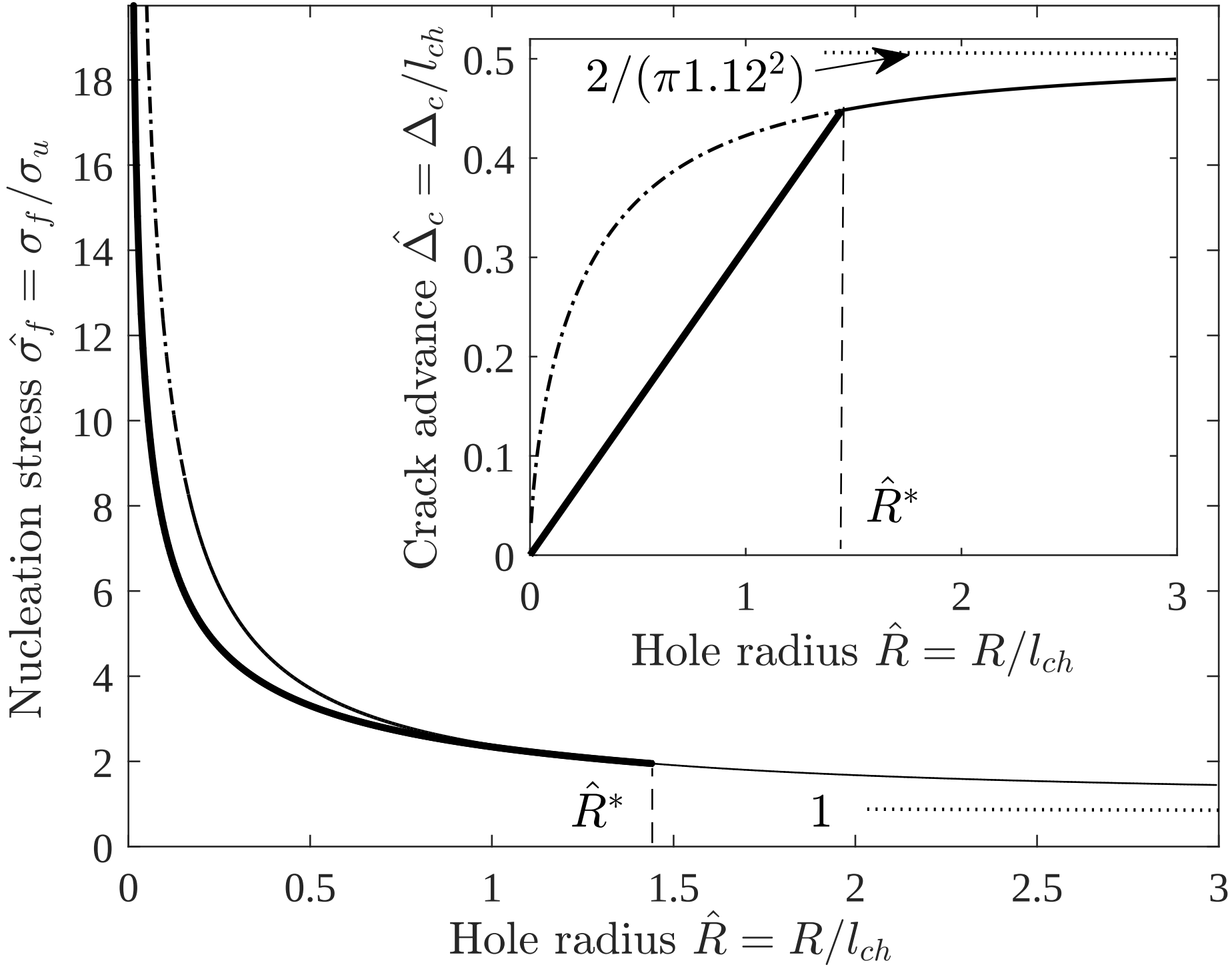
Nucleation stress $\hat{\sigma}_f = \sigma_f/\sigma_u$
Hole radius $\hat{R} = R/l_{ch}$
$\hat{R}^*$
1
Crack advance $\hat{\Delta}_c = \Delta_c/l_{ch}$
$2/(\pi 1.12^2)$
$\hat{R}^*$
Hole radius $\hat{R} = R/l_{ch}$

Fig. 5

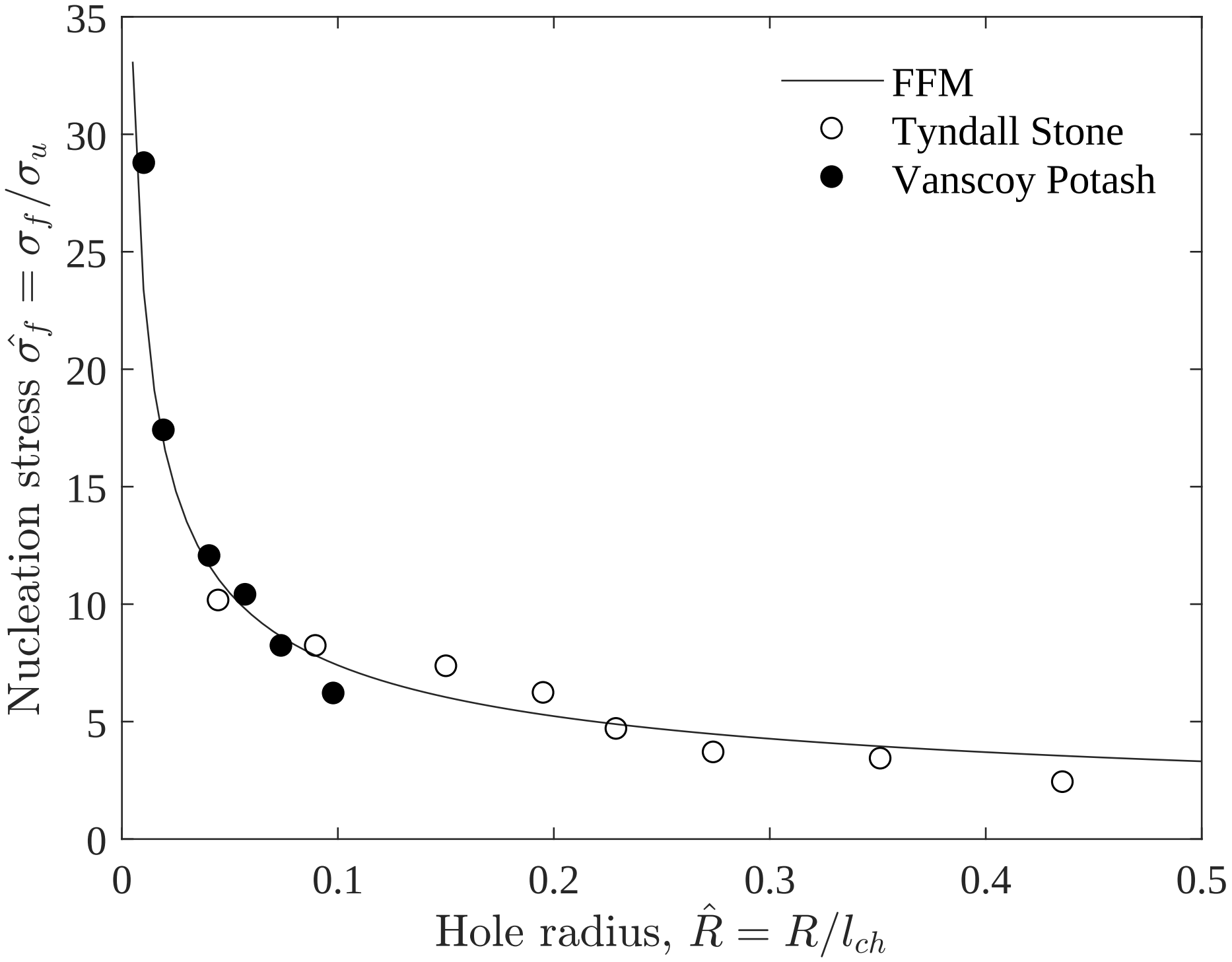
FFM
Tyndall Stone
Vanscoy Potash
Nucleation stress $\hat{\sigma}_f = \sigma_f/\sigma_u$
Hole radius, $\hat{R} = R/l_{ch}$
0
5
10
15
20
25
30
35
0
0.1
0.2
0.3
0.4
0.5

Fig. 6

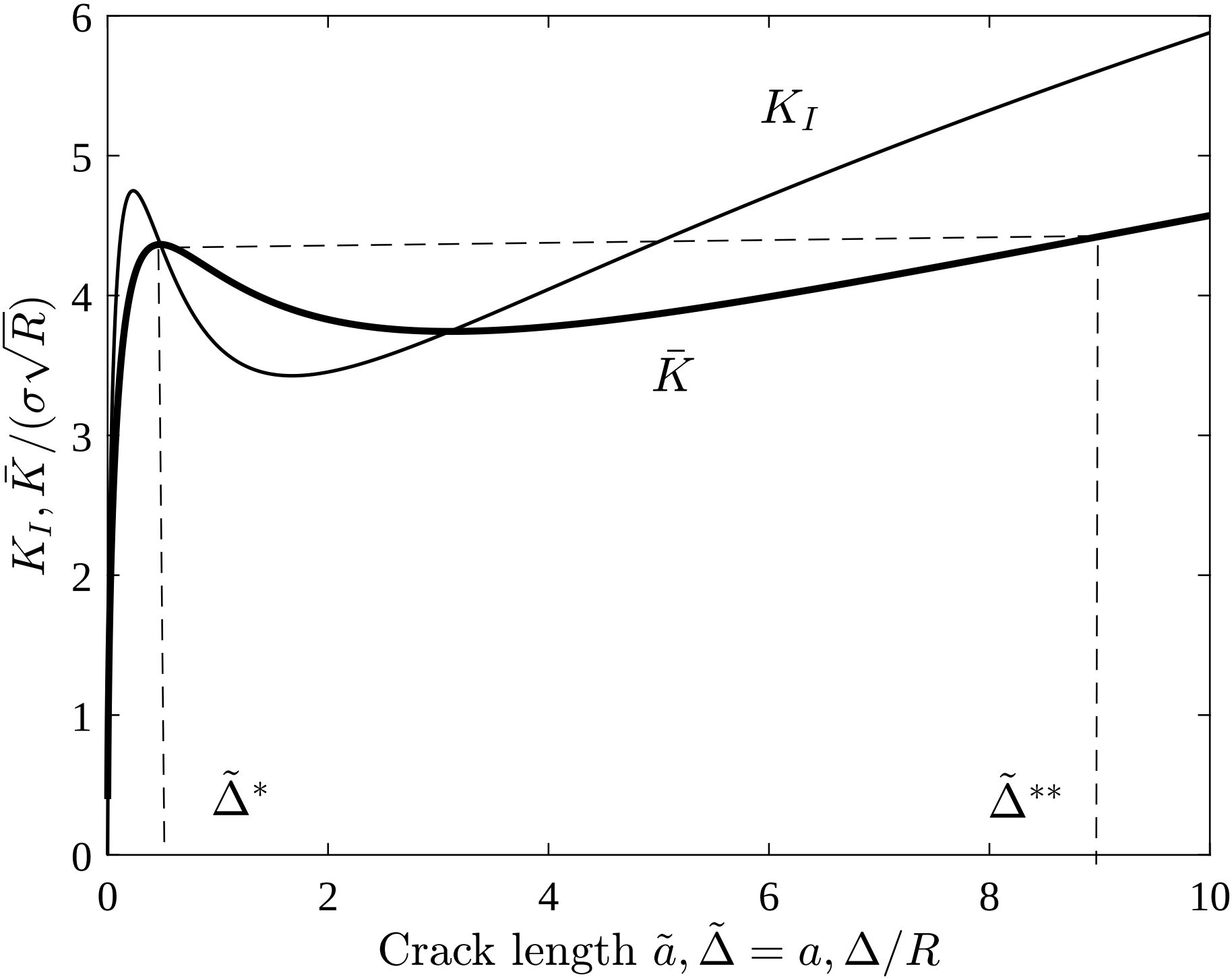
6
5
4
3
2
1
0
0
2
4
6
8
10
K_I
$\bar{K}$
$\tilde{\Delta}^*$
$\tilde{\Delta}^{**}$
$K_I, \bar{K}/(\sigma\sqrt{R})$
Crack length $\tilde{a}, \tilde{\Delta} = a, \Delta/R$

Fig. 7

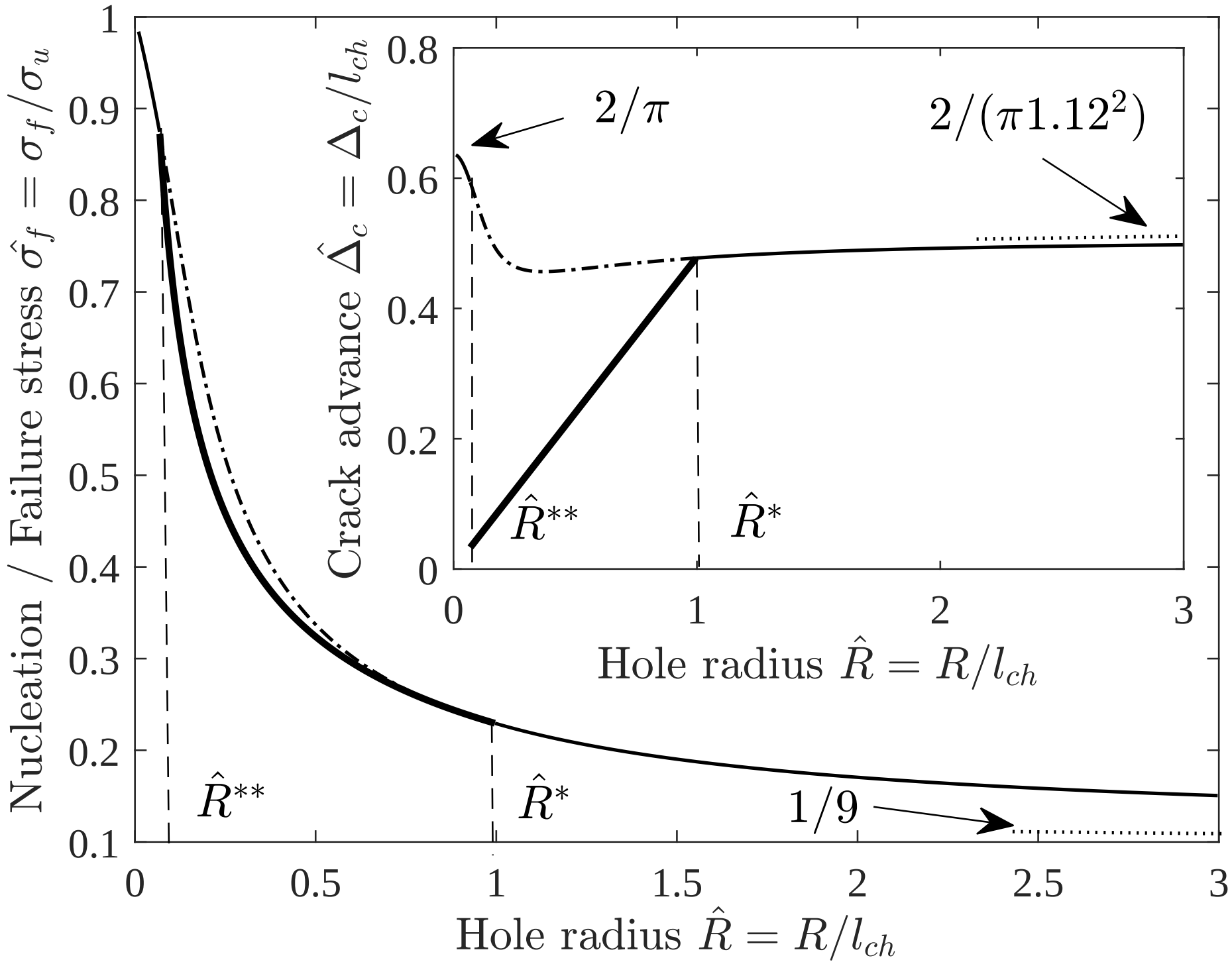
Nucleation / Failure stress $\hat{\sigma}_f = \sigma_f/\sigma_u$
Hole radius $\hat{R} = R/l_{ch}$
$\hat{R}^{**}$
$\hat{R}^{*}$
1/9
Crack advance $\hat{\Delta}_c = \Delta_c/l_{ch}$
$2/\pi$
$2/(\pi 1.12^2)$

Fig. 8

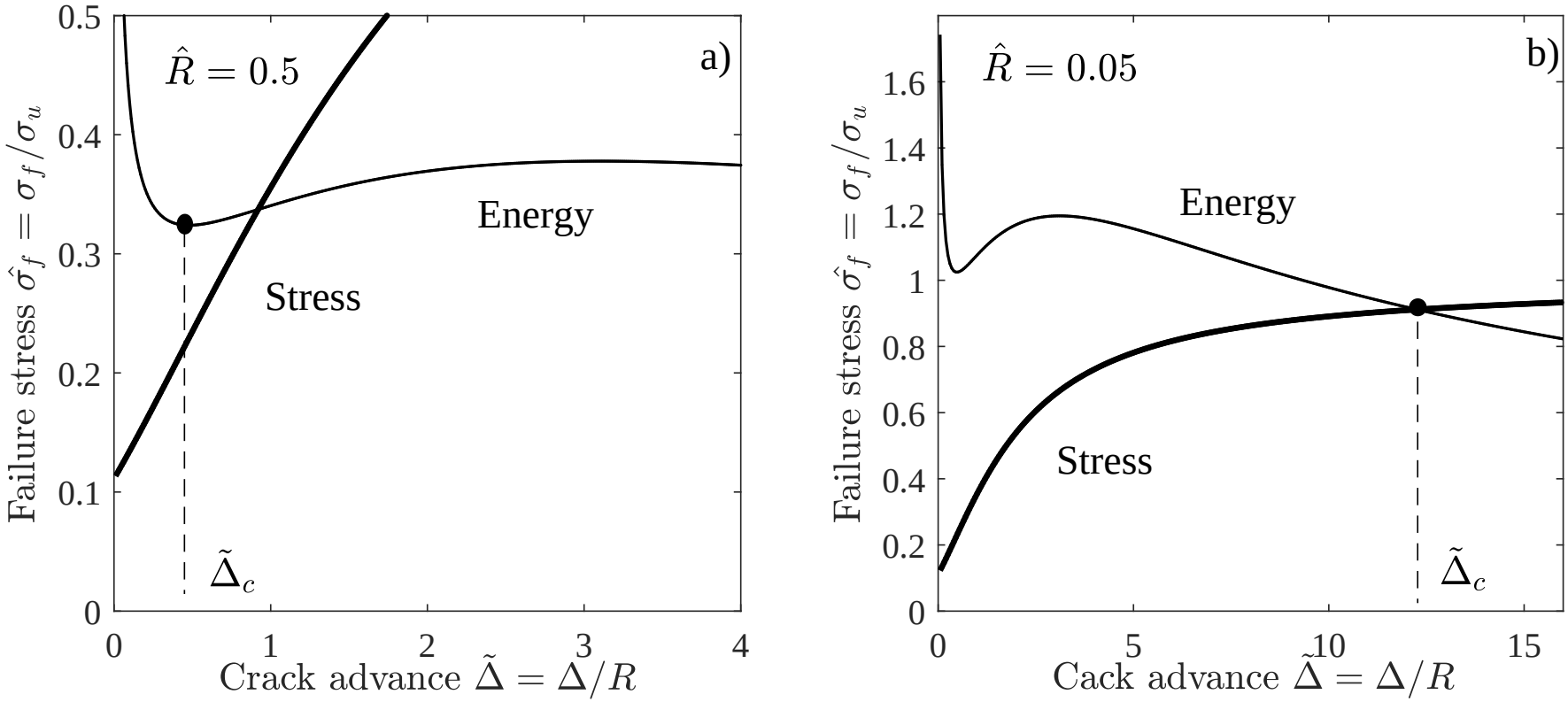
a)
$\hat{R} = 0.5$
Energy
Stress
$\tilde{\Delta}_c$
Failure stress $\hat{\sigma}_f = \sigma_f/\sigma_u$
Crack advance $\tilde{\Delta} = \Delta/R$
0
0.1
0.2
0.3
0.4
0.5
0
1
2
3
4
b)
$\hat{R} = 0.05$
Energy
Stress
$\tilde{\Delta}_c$
Failure stress $\hat{\sigma}_f = \sigma_f/\sigma_u$
Cack advance $\tilde{\Delta} = \Delta/R$
0
0.2
0.4
0.6
0.8
1
1.2
1.4
1.6
0
5
10
15

Fig. 9

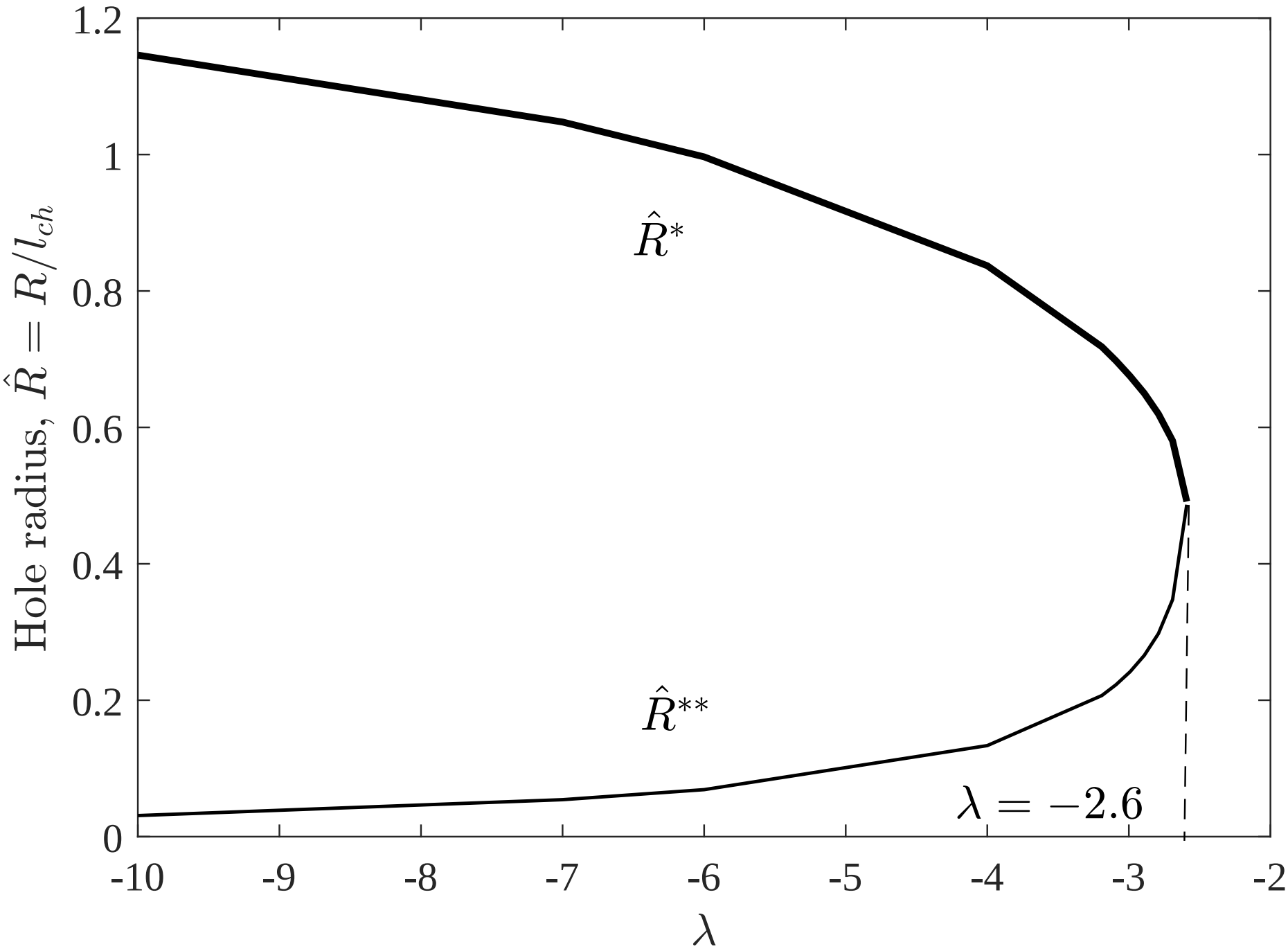
1.2
1
0.8
0.6
0.4
0.2
0
-10
-9
-8
-7
-6
-5
-4
-3
-2
λ
Hole radius, $\hat{R} = R/l_{ch}$
$\hat{R}^*$
$\hat{R}^{**}$
$\lambda = -2.6$

Fig. 10

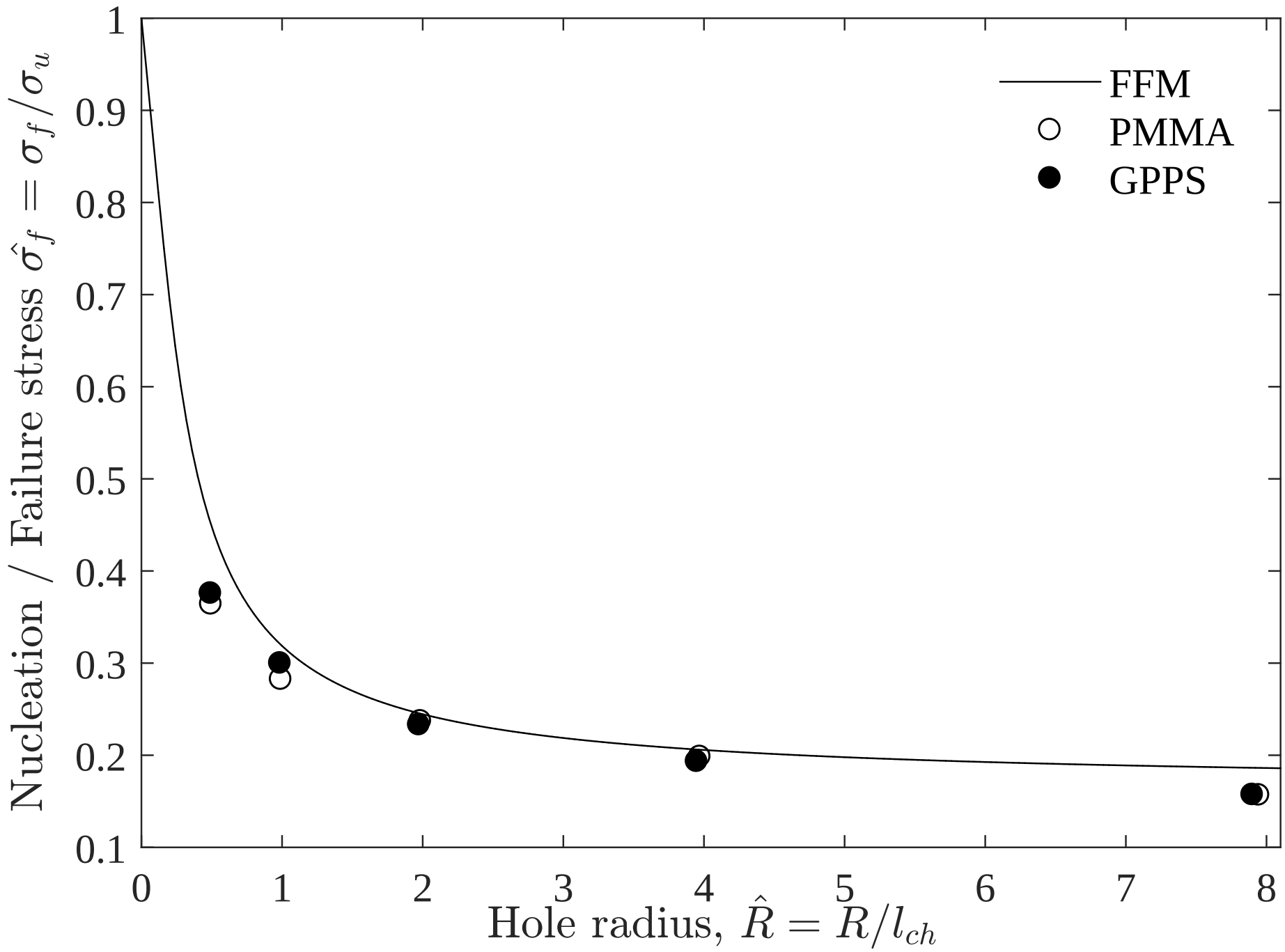
FFM
PMMA
GPPS
Nucleation / Failure stress $\hat{\sigma}_f = \sigma_f/\sigma_u$
Hole radius, $\hat{R} = R/l_{ch}$
1
0.9
0.8
0.7
0.6
0.5
0.4
0.3
0.2
0.1
0
1
2
3
4
5
6
7
8